Direct *in situ* measurement of coupled magnetostructural evolution in a ferromagnetic shape memory alloy and its theoretical modeling

Abhijit Pramanick,[1,*] Artur Glavic,[2,†] German Samolyuk,[3] Adam A. Aczel,[2] Valeria Lauter,[2] Haile Ambaye,[4] Zheng Gai,[5] Jie Ma,[2] Alexandru D. Stoica,[6] G. Malcolm Stocks,[3] Sebastian Wimmer,[7] Steve M. Shapiro,[8] and Xun-Li Wang[1,‡]

[1]*Department of Physics and Materials Science, City University of Hong Kong, Kowloon, Hong Kong SAR*
[2]*Quantum Condensed Matter Division, Oak Ridge National Laboratory, Oak Ridge, Tennessee 37831, USA*
[3]*Materials Science and Technology Division, Oak Ridge National Laboratory, Oak Ridge, Tennessee 37831, USA*
[4]*Research Accelerator Division, Oak Ridge National Laboratory, Oak Ridge, Tennessee 37831, USA*
[5]*Center for Nanophase Materials Sciences, Oak Ridge National Laboratory, Oak Ridge, Tennessee 37831, USA*
[6]*Chemical and Engineering Materials Division, Oak Ridge National Laboratory, Oak Ridge, Tennessee 37831, USA*
[7]*Department Chemie/Physikalische Chemie, Ludwig-Maximilians-Universität München, Butenandtstrasse 11, 81377 München, Germany*
[8]*Condensed Matter Physics and Materials Science Department, Brookhaven National Laboratory, Upton, New York 11973, USA*
(Received 27 June 2015; published 14 October 2015)

Ferromagnetic shape memory alloys (FSMAs) have shown great potential as active components in next generation smart devices due to their exceptionally large magnetic-field-induced strains and fast response times. During application of magnetic fields in FSMAs, as is common in several magnetoelastic smart materials, there occurs simultaneous rotation of magnetic moments and reorientation of twin variants, resolving which, although critical for design of new materials and devices, has been difficult to achieve quantitatively with current characterization methods. At the same time, theoretical modeling of these phenomena also faced limitations due to uncertainties in values of physical properties such as magnetocrystalline anisotropy energy (MCA), especially for off-stoichiometric FSMA compositions. Here, *in situ* polarized neutron diffraction is used to measure directly the extents of both magnetic moments rotation and crystallographic twin-reorientation in an FSMA single crystal during the application of magnetic fields. Additionally, high-resolution neutron scattering measurements and first-principles calculations based on fully relativistic density functional theory are used to determine accurately the MCA for the compositionally disordered alloy of $Ni_2Mn_{1.14}Ga_{0.86}$. The results from these state-of-the-art experiments and calculations are self-consistently described within a phenomenological framework, which provides quantitative insights into the energetics of magnetostructural coupling in FSMAs. Based on the current model, the energy for magnetoelastic twin boundaries propagation for the studied alloy is estimated to be $\sim$150 kJ/m^3.

I. INTRODUCTION

The coupling between magnetism and electronics has been intensively studied in the last decade, while the effects of magnetostructural interactions have received relatively less attention. Understanding such interactions are nevertheless critical for controlling the properties of many functional materials such as ferromagnetic shape memory alloys (FSMA) [1], magnetostrictive heterostructures [2], and magnetoelectric multiferroics [3]. In these materials, the magnetic moment is strongly coupled to the crystal lattice, and therefore the rotation of the magnetic moments by an external driving force can lead to a consequent rearrangement of crystal lattice in the form of twin reorientation. As a result, strong coupling between magnetic moments and crystallographic twin orientations can give rise to many interesting effects, such as large magnetic-field-induced strains and memory effects in resistivity and magnetization, with potential applications in smart actuators and information storage [4–7]. Therefore, from both fundamental and technological viewpoints, it is of

utmost importance to be able to quantitatively determine and model both magnetic moment rotation and twin reorientation, which can occur simultaneously under the application of magnetic fields. Here, we address this challenging issue using the exemplary case of a Ni-Mn-Ga FSMA.

FSMAs are known to exhibit large magnetic-field-induced strains: for example, a maximum strain of $\sim$10% has been reported for Ni-Mn-Ga [8–12]. The underlying mechanism for such large strains is a reorientation of crystallographic twins when a magnetic field is applied away from the direction of the easy magnetization axis, which proceeds through the nucleation and propagation of twin boundaries [13,14]. The sequence of magnetostructural events under incremental magnetic fields are principally determined by a delicate balance between the following three competing energies: the Zeeman energy, which tends to align the magnetic moments along the direction of the magnetic field; the magnetocrystalline anisotropy (MCA) energy, which tends to keep the magnetic moment parallel to the easy magnetization axis of the crystal lattice; and the energy required to nucleate and propagate twin boundaries [15,16]. In addition, magnetostatic energy associated with demagnetizing fields could also play an important role if the dimension of the sample along which the magnetic field is applied is sufficiently small. At low fields, the magnetic moments can rotate from the easy magnetization axis as long as the net cost for doing so from the first two

_____

*abhijit.pramanick@gmail.com
†Present address: Laboratory for Neutron Scattering and Imaging, Paul Scherrer Institut, Switzerland.
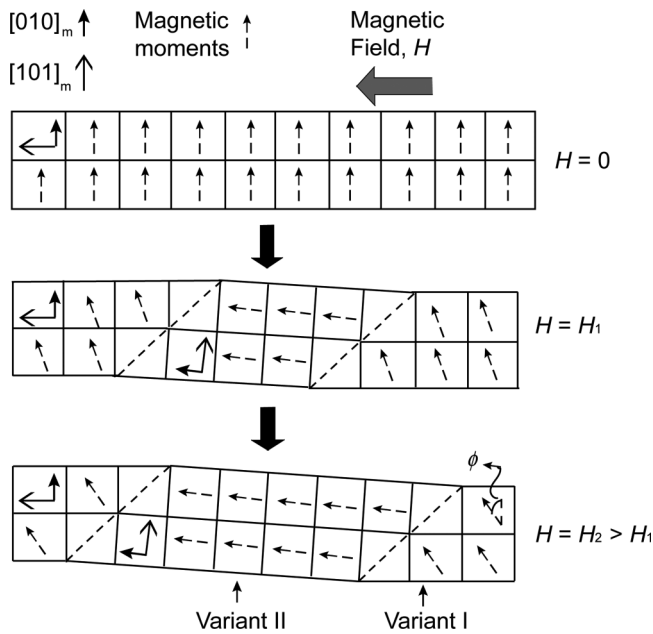‡xlwang@cityu.edu.hk

FIG. 1. A schematic illustration of induced magnetostructural changes in FSMA single crystals under increasing magnetic field strengths of $0 < H_1 < H_2$, which includes a rotation of magnetic moments in variant I by angle ϕ and reorientation of a fraction of twins from variant I to variant II.

energy terms is less than the energy required for twin boundary nucleation and propagation [17]. Above a certain threshold field, however, it becomes energetically more favorable to initiate twin reorientation, so that an increasing number of magnetic moments can be co-aligned with the magnetic field direction and the overall energy of the system is lowered. These changes are schematically illustrated in Fig. 1 for the general case of a microstructure with two twin variants. In order to elucidate the delicate balance between these competing energy components in an FSMA, it is critical to be able to quantify the rotation of the magnetic moment vectors and the volume fraction of reoriented twins, both of which could occur simultaneously under the application of magnetic fields. This is also an important technological issue, since the relative domination of either twin reorientation or magnetic moment rotation determines how much force or energy density can be obtained from FSMA components during their magnetic actuation [18,19].

In the past, microstructural investigations of magnetic shape memory effect have almost entirely focused on martensitic twin reorientation [20–24]. While these studies provided valuable physical insights into the phenomenon of twin boundary motion, the simultaneous rotation of magnetic moments has been addressed only qualitatively. Experimentally, it is challenging to characterize the rotation of magnetic moments in an evolving twin microstructure. This is because of contributions from multiple mechanisms, including magnetic moment rotation, twin reorientation, and interactions among ferromagnetic domains and twins, all of which are convoluted within the magnetization curve measured for a bulk sample, and it becomes difficult to distinguish between their individual contributions [17,25–28]. A microscopic probe, which selec-

tively measures the orientations of magnetic moments within the differently oriented twin variants, is therefore required. In this respect, some insights were provided by Lorentz microscopy studies, which looked at ferromagnetic domain wall evolution under applied magnetic fields [29]. However, due to the technical constraints of applying a high magnetic field within a transmission electron microscope, the applied magnetic fields for Lorentz microscopy studies were limited to a maximum of 0.05 T, which is less than the threshold field for twin reorientation (>0.3 T) [9]. At the same time, phenomenological models for describing correlation between rotation of magnetic moments and twin reorientation fraction also faced limitations due to uncertainties in the value of material properties such as MCA, especially for off-stoichiometric FSMA compositions, and therefore they could only be qualitative at present [15,16,30,31]. Recent advances in phase field modeling have shown potential for more quantitative estimates of magnetic moment rotation and twin reorientation in FSMAs [32–34], although their accuracies are still a subject of debate.

Here, using a state-of-the-art experimental technique for polarized neutron diffraction at a time-of-flight instrument, we have directly measured both rotation of magnetic moments and crystallographic twin reorientation in a single crystal of martensitic Ni-Mn-Ga during the application of magnetic fields. The material is an off-stoichiometric $Ni_2Mn_{1.14}Ga_{0.86}$ alloy with a 5M monoclinic crystal structure [35], the further details for which are provided in the next section. The martensitic transformation temperatures of the alloy are $T_M = (M_s + M_f)/2 = 321$ K, $T_A = (A_s + A_f)/2 = 327$ K; the Curie temperature is $T_C = 372$ K [35]. All materials characterization measurements were done at the temperature of 250 K. The experimentally observed correlation between volume fraction of reoriented twins and rotation of magnetic moments is consistently modeled within a phenomenological framework, by incorporating values of MCA that were determined from both high-resolution neutron spin wave measurements as well as from first-principles calculations based on fully relativistic density functional theory. This enabled quantitative insights into the energetics of the different mechanisms leading to large magnetic-field-induced strains in FSMAs. A noteworhty finding here is that the energy for magnetoelastic twin boundaries propagation is ~ 150 kJ/m^3, which could be an important guiding factor for predictive control of twin boundary motion through microstructural modifications or external restoring forces.

II. MATERIALS SPECIFICATIONS

High-quality single crystal FSMA samples of Ni-Mn-Ga having a single twin variant were obtained from Goodfellow Corporation. The crystals showed good surface uniformity and had a shining texture. In the martensitic state, the alloy has a 5M modulated structure with lattice parameters, a = 4.255 Å, b = 5.613 Å, and c = 4.216 Å [35]. The nominal composition of the alloy obtained is $Ni_{50}Mn_{28}Ga_{22}$, as described by the vendor and further verified by us from Energy Dispersive Spectrometry analysis with a scanning electron microscope.

The crystallographic indices for the plane normals and the Bragg diffraction peaks used in this paper follow the simplified monoclinic indices as was reported earlier [36]. The indices in the simplified monoclinic notation can be interchanged with those of the pseudocubic notation through the following relations: $[001]_m \| [1\bar{1}0]_c$, $[100]_m \| [110]_c$, and $[010]_m \| [001]_c$, where the subscripts m and c refer to the monoclinic and the pseudocubic notations, respectively [35].

III. NEUTRON DIFFRACTION MEASUREMENT OF MAGNETOSTRUCTURAL CHANGES

The unique advantages provided by polarized neutron diffraction at a spallation source with regard to the characterization of magnetic-field-induced rotation of electron spins within the material components were recently demonstrated in Ref. [37]. Neutrons carry a magnetic moment of their own and therefore act as a probe for the microscopic magnetic moments. Uniquely, in a time-of-flight measurement, the diffraction peaks originating from the differently oriented twin variants are separated in time and space, which enables the simultaneous measurements of different twin-specific reflections in each individual measurement frame using an area detector. The Magnetism Reflectometer (MR) time-of-flight spectrometer at the Spallation Neutron Source uses a coupled hydrogen moderator optimized for higher intensity and a good wavelength resolution. The instrument also includes a position sensitive detector with adequate angular resolution to measure diffraction peaks over a relatively broad range of wave vectors. The combination of these instrumental features at the MR enabled us to undertake diffraction measurements of sequential magnetostructural changes in FSMAs under stepwise increments of magnetic fields. The principle for polarized neutron diffraction from magnetically ordered crystals is well established [38], and its application at a spallation source for the characterization of a ferromagnet under incremental magnetic fields was covered in a previous publication [37]. Further building up on these initial studies, here, we applied a full-polarization analysis of the neutron diffraction intensities from a Ni-Mn-Ga single crystal in order to quantitatively determine the different magnetic-field-induced changes within the material.

The sample used for *in situ* polarized neutron diffraction was in the form of a flat plate with dimensions of 5 mm by 2 mm by 25 mm, with the longer dimension parallel to the direction of the applied magnetic field. Prior to the neutron diffraction measurements, we obtained a single variant state by saturating the magnetization of the sample under a field of 1.15 T applied along the normal to the 5 mm by 25 mm face of the crystal. Subsequent to that, the normal to the larger face of 5 mm by 25 mm was parallel to the [010] crystallographic direction, while the magnetic field was applied parallel to the orthogonal direction of [101]. The sample was mounted inside a square bracket using cotton wools for support, so that minimum mechanical constraint was applied during the generation of magnetic-field-induced strains. The magnetic field increments for the *in situ* experiment were chosen to capture the transitional states close to threshold fields for twin reorientation and were based on previous macroscopic magnetic susceptibility measurements. Diffraction patterns were
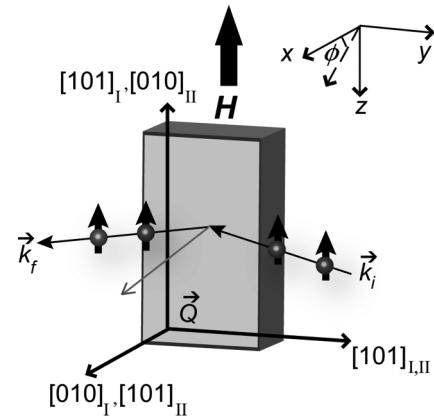

FIG. 2. Schematic representation of experimental setup for *in situ* polarized neutron experiment. $\vec{k}_i$ and $\vec{k}_f$ are the vectors representing the initial and the diffracted neutron beams, respectively. The area detector is placed so as to measure the reflection with scattering vector $\vec{Q}_{020}$ from twin variant I, and reflection with scattering vector $\vec{Q}_{101}$ from twin variant II. The magnetic field is applied parallel to the vertical $\vec{z}$ axis, which causes the electron spins to rotate in the $\vec{x}-\vec{z}$ plane.

collected using spin-down (I^-) and spin-up (I^+) polarized neutrons at each increment in applied magnetic field. The scattering intensities I^- and I^+ were collected in alternation by switching the neutron polarization every 60 s. The final pattern for each spin state was obtained by integrating over a total time period of 7 min.

The geometry of the diffraction experiment is shown in Fig. 2. We consider twin variants I and II which have either their [010] or [101] crystal axis oriented within the scattering plane spanned by the accessible scattering vectors $\vec{Q} = \vec{k}_i - \vec{k}_f$. The area detector was strategically placed so that both reflections (020) from variant I and (101) from variant II are captured at the same time, which is possible due to the close proximity of their respective d-spacings. The volume fractions of the two twin variants II and I are given by f and $(1-f)$, respectively, with the initial state given by $f = 0$. The incident beam is polarized with the polarization vector $\vec{P}$ parallel or antiparallel to the $\vec{z}$ direction of the laboratory coordinate system and perpendicular to the scattering plane. The diffracted neutrons were recorded in time-of-flight mode and their wavelengths were subsequently obtained from the total flight path. In the two-dimensional maps shown in Fig. 3, the Bragg peaks were measured for wavelengths and the diffraction angles which satisfied the condition $|\vec{Q}_B| = 4\pi \sin\theta/\lambda = $ constant. Using the Bragg condition, the two-dimensional diffraction data were subsequently transformed to obtain diffracted intensities for values of $|\vec{Q}_B| = $ constant [37].

Ideally for this geometry, there is no spin-flip and the scattering cross sections are given by

$$I^+ = \left(\frac{d\sigma}{d\Omega}\right)_{u \to u} \propto (\bar{b} - C^z)^2 \quad \text{and}$$

$$I^- = \left(\frac{d\sigma}{d\Omega}\right)_{v \to v} \propto (\bar{b} + C^z)^2 \tag{1}$$

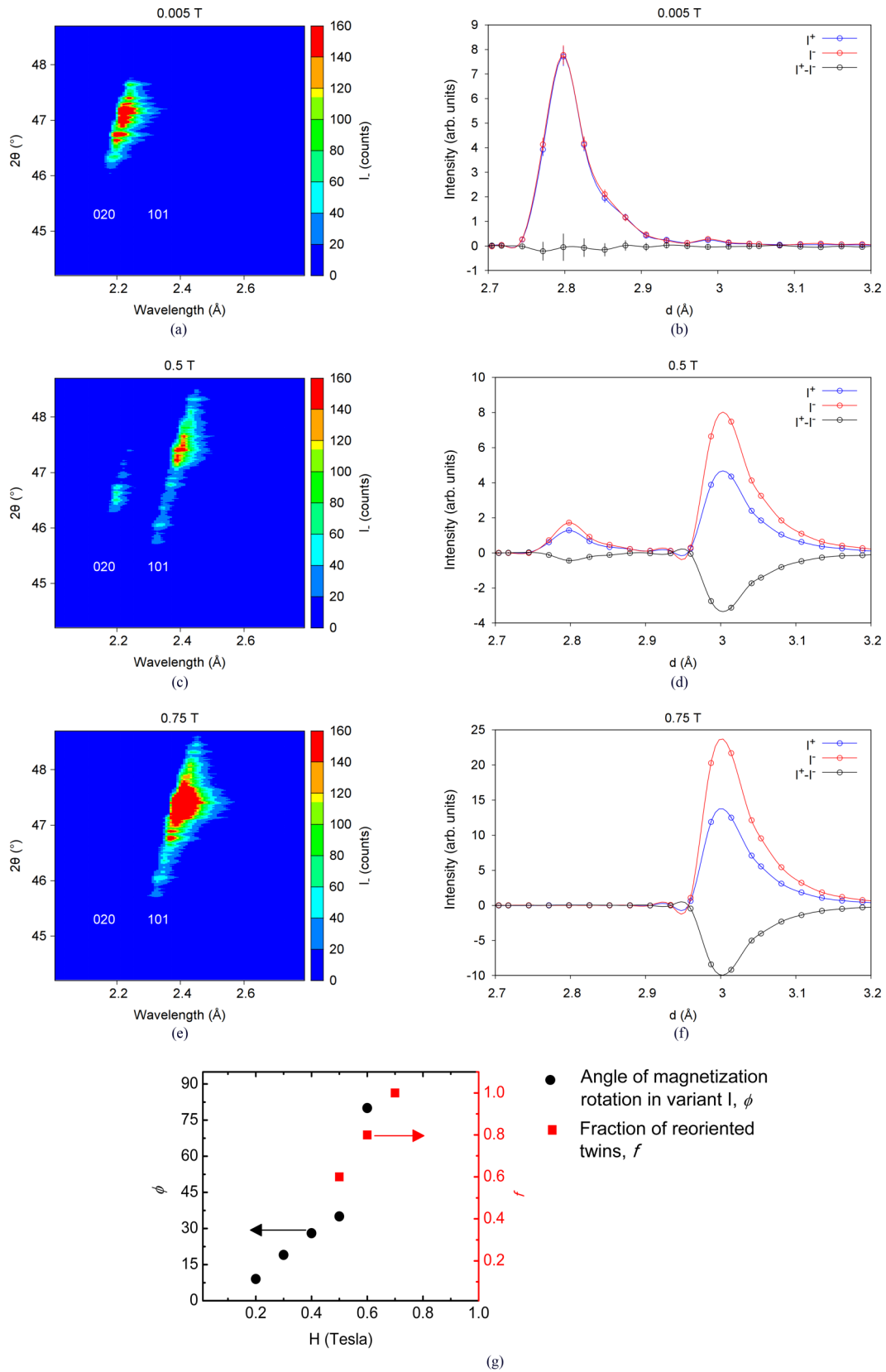$$\text{where} \quad C^z = \frac{1}{2}\gamma r_0 g F_M \langle \vec{S}^z \rangle. \tag{2}$$

FIG. 3. (Color online) Magnetic field-induced magnetostructural changes in Ni-Mn-Ga single crystal measured with polarized neutron diffraction: (a), (c), (e) measured diffraction patterns on the area detector for applied fields of 0.005 T, 0.5 T, and 0.75 T, respectively; (b), (d), (f) the same information as above presented as one-dimensional plots as function of lattice spacings, d, after integration over the two-dimensional diffraction patterns; (g) changes in volume fraction of reoriented twins, f, and the rotation angle of magnetic moments ϕ as functions of $\vec{H}$.

In Eq. (1), $\bar{b}$ is the nuclear unit-cell structure factor for a particular reflection with scattering vector $\vec{Q}$. In Eq. (2), $\gamma = 1.913$ is the neutron gyromagnetic ratio, $r_0 = 2.818 \times 10^{-15}$ m is the classical radius of the electron, g is the Lande splitting factor, F_M is the magnetic structure factor of the magnetic atoms, and $\langle \vec{S}^z \rangle$ is the mean component of the electron spins parallel to $\vec{z}$. The symbols u and v denote the spin-up and spin-down states of the polarized neutrons, respectively. $\langle \vec{S}^z \rangle$ is proportional to $\sin\phi$, where ϕ is equal to the angle between the easy magnetization axis [010] and the direction of the magnetic moment, as illustrated in Fig. 2. However, even though there is no spin-flip scattering for magnetic moments that are (anti-)parallel to the neutron polarization or the scattering vector, some depolarization of the neutron beam can occur within the sample due to a precession of the neutron spins in the internal field of the sample, which consequently can lead to a departure from the ideal diffracted intensities given in Eq. (2). The depolarization phenomenon is particularly prominent at small magnetic fields, when $\langle \vec{S}^z \rangle$ is perpendicular to the applied field direction. In order to account for neutron beam depolarization within the sample, we therefore measured the neutron scattering intensities with a full polarization analysis, from which we could determine the depolarization factor for the neutron beam (see Supplemental Material [39] and Ref. [40]). In all subsequent calculations presented below, we have used intensities that have been corrected for neutron beam depolarization.

Figure 3 shows the neutron scattering intensities measured *in situ* under the application of magnetic fields from the Ni-Mn-Ga single crystal, which have been corrected for neutron beam depolarization as described above. The crystal has a single twin variant in its initial state. For a minimum applied field of 0.005 T, no significant difference in the diffracted intensities with the spin-up (I^+) and the spin-down (I^-) states is noted for the (020) reflection, which is expected for $\langle \vec{S}^z \rangle \approx 0$. With increasing magnetic fields up to 0.4 T, an increase in difference between I^+ and I^- for the (020) reflection could be noted, which is caused by nonzero values of $\langle \vec{S}^z \rangle$ as a result of rotation of the electron spins towards $-\vec{z}$ in the $\vec{x} - \vec{z}$ plane. When the applied magnetic-field reaches 0.5 T, the (101) diffraction peak appears in addition to the (020) peak, indicating reorientation of a fraction of twins from variant I to II (additional diffraction peaks due to the presence of a third or additional variants were not observed in the experiment). For applied fields greater than 0.7 T, only the (101) peak is measured, indicating complete reorientation of all the structural twins at these fields. A large difference between the I^+ and I^- intensities for the (101) reflection at all field values is consistently observed, indicating that the magnetic moments in the reoriented twin variants or variant II are always nearly parallel to the applied field direction.

The volume fraction of the reoriented twins f is calculated from

$$f = \frac{I_{101}}{I_{101} + k I_{020}}, \qquad (3)$$

where I_{101} and I_{020} are the nuclear components of the diffracted intensities corresponding to the (101) and (020) reflections, respectively. The nuclear structure factors for the two reflections should be equal, that is, $(F_{101}/F_{020})^2 \approx 1$ [14]. In addition, the factor k is included in Eq. (3) to account for the wavelength dependence of intensities for the incoming beam spectra.

Next, the angle ϕ between the magnetic moments and the easy magnetic axis [010] is calculated by a comparative analysis of $(I^-/I^+)_{\vec{H}}$ measured for an applied field of $\vec{H}$ with $(I^-/I^+)_{\text{sat}}$, where the subscript *sat* denotes saturation field, that is, when $\langle \vec{S}^z \rangle$ is saturated along the direction orthogonal to the scattering vector $\vec{Q}$. Note that the magnetic moment is aligned along [010] under equilibrium conditions. Therefore, $(I^-/I^+)_{\vec{H}} = (I^-/I^+)_{\text{sat}}$ for reflection (020) when $\phi = 90°$; while $(I^-/I^+)_{\vec{H}} = (I^-/I^+)_{\text{sat}}$ for reflection (101) when $\phi = 0°$. The value for $(I^-/I^+)_{\text{sat}}$ was obtained from Fig. 3(f) as well as from previous measurements presented in Ref. [37]. From Eqs. (1) and (2) and for constant $\bar{b}$, we find that $\frac{(I^-)^{1/2} - (I^+)^{1/2}}{(I^-)^{1/2} + (I^+)^{1/2}} \propto C^z$. In other words, the factor $\frac{(I^-)^{1/2} - (I^+)^{1/2}}{(I^-)^{1/2} + (I^+)^{1/2}}$ is directly related to $\langle \vec{S}^z \rangle$ or ϕ. For the (020) reflection originating from twin variant I, this factor is equal to zero when $\langle \sin\phi \rangle = 0$, and is maximum when $\langle \sin\phi \rangle = 1$ corresponding to $(I^-/I^+)_{\vec{H}} = (I^-/I^+)_{\text{sat}}$. Since, we know the value of $(I^-/I^+)_{\text{sat}}$, the values for ϕ at different field strengths $|\vec{H}|$ within twin variant I can be calculated accordingly from the measured diffraction intensities of the (020) reflection using a simple scaling relation.

Evolution of the volume fraction of variant II or f and the rotation angle ϕ for magnetic moments within variant I, as functions of magnetic field strengths are shown in Fig. 3(g). The measured ϕ for applied fields of H $\leqslant$ 0.4 T are in line with the predictions from phase field models for small external stresses (below 0.6 MPa) [32–34]. Most interestingly, a partial reorientation of a fraction of twins (f) from variant I to variant II is observed for applied fields of 0.5 T and 0.6 T, which occurs simultaneously with a rotation of the magnetic moments within the original twin variant I. Both of these phenomena contribute to the magnetization curves measured for a bulk sample, although it is only through unique microscopic-level characterization using polarized neutron diffraction, such as provided here, that their individual contributions could be quantitatively distinguished. Finally, upon further increase of magnetic field to 0.7 T, only the (101) diffraction peak remains as shown in Figs. 3(e) and 3(f), which indicates that all the twin variants at this field have reoriented from variant I to II. A large scale reorientation of twin variants above a threshold field of 0.4 T observed here is consistent with a discontinuous rise in the magnetic-field-induced strains typically observed for field strengths between 0.3 T and 0.5 T in Ni-Mn-Ga single crystals while starting from a single variant state [41–43]. Therefore, the current measurements uniquely enable a direct quantitative determination of stepwise increments in *both* twin reorientation fractions and rotation angle of magnetic moments with increasing magnetic fields, which has been hitherto impossible with other characterization techniques. This enabled a quantitative analysis of the relative

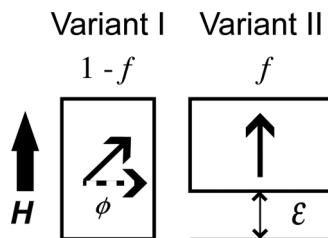## Variant I　　Variant II
$1 - f$　　　　f

FIG. 4. The total free energy of the system is calculated for a model microstructure with two twin variants whose relative configurations are illustrated above. Note f is the volume fraction of twins reoriented from variant I to variant II, ϕ is the angle of rotation of the magnetic moments in variant I, and ε is the spontaneous strain generated due to twin reorientation.

energetics of the different magnetostructural phenomena, as further described below.

IV. PHENOMENOLOGICAL MODEL FOR MAGNETOSTRUCTURAL EVOLUTION

A. Equation for free energy density of a twinned microstructure

In order to develop an in-depth physical understanding of the underlying energetics for magnetostructural evolution in FSMAs, we seek a phenomenological framework from which the general correlation between f and ϕ can be determined in a self-consistent manner. For this, we calculated the total free energy density for a model microstructure consisting of two twin variants having their [010] axes orthogonal to each other, as shown in Fig. 4. The inclusion of only two variants is justified here since only two distinct diffraction spots could be observed in the neutron diffraction experiment. The presence of two twin variants is also typically observed during magnetic-field-induced twin reorientation while starting from a single variant state [44]. For an applied magnetic field of strength H, the total free energy density of the system U can be given by,

$$U = -M_s H \times [f + (1 - f)\sin\phi] + (1 - f)K_u\sin^2\phi + E_{\text{int}}$$

(4)

where M_S is the magnetic moment at saturation, K_u is the MCA of the low-temperature martensite phase and E_{int} is an interfacial energy term which corresponds to the energy cost for nucleation and propagation of twin boundaries [16,45,46]. In the above expression, the demagnetization energy is excluded since the dimension of the sample along the magnetic field direction (25 mm) is much longer than the thickness of the sample (2 mm). The intrinsic material constants of M_S and K_u of the martensite phase at 250 K were evaluated from measurement of magnetization curves for a bulk crystal, further measurement of spin-waves with neutron scattering, and fully relativistic first-principles calculations, as explained in the next Sec. IV.B.

For a specific volume fraction of reoriented twins f, the equilibrium value for ϕ is obtained when $\partial U/\partial\phi = 0$, which defines the correlation between f and ϕ. For this purpose, the calculation of the free energy density curves as a function of applied magnetic field magnitudes is described in Sec. IV.C. The predicted values of ϕ are then compared with direct experimental observations for self-consistency.
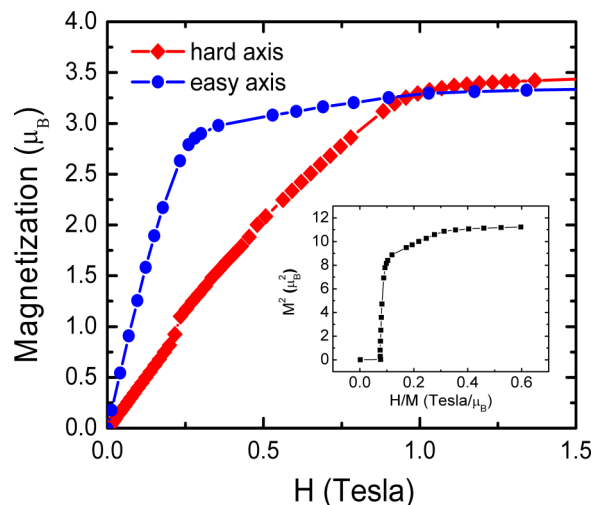

FIG. 5. (Color online) Magnetization curves measured along the easy [010] and the hard [101] magnetization axes for the Ni-Mn-Ga alloy at 250 K. The corresponding Arrott plot for the magnetic susceptibility along the easy axis is shown in the inset.

The term E_{int} corresponds to the energy term for twin boundary propagation, which incorporates within it the effects of microscopic features such as dislocations and other types of defects. In order to estimate E_{int} from the experimentally observed magnetic-field-induced magnetostructural changes in the FSMA crystal, we used the following approach. For an applied field of $H = 0.5$ T, we determined $f \sim 0.6$. Therefore, since E_{int} is finite for $f \sim 0.6$ but is zero for $f = 0$, the difference $\Delta U = [U(f = 0.6) - U(f = 0)]$ refers to the interfacial energy E_{int} spent for the reorientation of $f = 0.6$ fraction of the twin variants. The calculation of E_{int} is described in Sec. IV.D.

While free energy expression similar to Eq. (4) was used earlier to describe the phenomenon of twin reorientation in FSMAs [45,46], the uniqueness in our approach is that we have incorporated information about both f and ϕ from direct experimental observations, which helped us to check for self-consistency and furthermore enabled evaluation of E_{int} from this model.

B. Evaluation of material constants M_S and K_u

The value of M_S (or the saturation magnetic moment) at 250 K is determined from the measured magnetization curves as shown in Fig. 5. The measurements were taken with a superconducting quantum interference device (SQUID)–based Quantum Design Magnetic Property Measurement System. The sample used for the measurement was a single variant 2 mm by 2 mm by 2 mm crystal of $Ni_2Mn_{1.14}Ga_{0.86}$. The Arrott plot for the square of magnetization M^2 with respect to H/M is shown in the inset, from which it could be observed that saturation magnetization M_S is reached for values of $H/M > 0.5$ (Tesla/μ_B). Accordingly, we obtained $M_S \sim 3.5\,\mu_B$/formula unit, which is consistent with values reported earlier for T $\leqslant$ 300 K [25,35].

However, the value for K_u or MCA is less certain for Ni-Mn-Ga alloys, especially for off-stoichiometric alloy compositions. Estimates of $K_u \sim 25-75\,\mu eV$ per formula unit in the tetragonal martensite phase of Ni-Mn-Ga alloys were

made earlier from magnetization measurements [17,27], which were lower by a factor of 2.5–3.5 than the corresponding value of $\sim 150\,\mu$eV [per formula unit] reported from first-principle calculations and spin wave measurements with neutron scattering [47,48]. In view of such conflicting findings, we have re-examined the value of K_u for the current alloy.

First, we used the method described by Heczko *et al.* in which K_u is considered numerically equivalent to the area enclosed within the magnetization curves measured along the easy and the hard magnetization axes [17]. Using this method, the data shown in Fig. 5 yields $K_u \sim 40\,\mu$eV. However, determination of K_u from magnetization curves measured on a bulk crystal sample could be open to uncertainties. There are various possible reasons for this. First, the demagnetization energy plays a significant part at small fields, which is responsible for a rising slope prior to the attainment of the saturation magnetization along the easy magnetization axis. Moreover, there are likely contributions from various nonintrinsic microscopic or external influences such as mechanical constraints, minute fraction of secondary twin variants or austenite phase, and/or microscopic magnetic exchange couplings between the different twins or domains. We therefore chose to determine K_u directly from measurement of spin wave dispersions in the material and, moreover, to independently verify the same with first-principles calculations.

The value of K_u can be obtained directly from measurements of spin wave dispersion using inelastic neutron scattering [48,49]. The low-energy spin wave dispersion of a ferromagnet can be described by,

$$\hbar\omega(q) = \Delta + Dq^2 + \cdots \qquad (5)$$

where $\hbar\omega(q)$ is the energy of the magnetic spin wave for a wave vector $\vec{q}$, Δ is the energy gap of the dispersion at the zone center (ZC) $q = 0$, and D is the magnetic exchange stiffness constant. Δ is numerically equal to the intrinsic value of K_u of a material. In Eq. (5), the terms for higher orders of q can be ignored in the long wavelength limit of the spin waves.

The spin wave dispersion in the alloy $Ni_2Mn_{1.14}Ga_{0.86}$ was measured by inelastic neutron scattering at the Cold Triple-Axis Spectrometer (CTAX) located at the High Flux Isotope Reactor (HFIR) of the Oak Ridge National Laboratory. Four single crystal samples, each of dimensions 5 mm by 5 mm by 5 mm, were coaligned on a stage for neutron scattering spin wave measurements. Prior to coalignment of the crystals for neutron scattering measurements, each crystal was prepared into a single variant martensite state by subjecting it to a saturating magnetic field of 1 T. The measurements were made at the HFIR of Oak Ridge National Laboratory, using CTAX, with guide-open-80′-open collimation. The energy of the scattered neutrons was fixed at $E_f = 5$ meV for energy transfers of $\geqslant 1$ meV and $E_f = 3$ meV for lower energy transfers. Higher order contamination was removed from the beam by a cooled Be filter placed between the sample and analyzer.

The neutron scattering measurements were performed by scanning along the high symmetry direction of [111] for constant values of energy transfers of $E_i - E_f$. Representative scans are shown in Figs. 6(a) and 6(b). The transverse acoustic phonon is anomalously softened for the [111] direction in the martensitic phase (or [110] direction in the cubic notation), which gives a lower slope for dispersion in q [50].

Therefore this direction is preferred here for measuring the spin wave dispersion so that possible intermixing of phonons and magnons in the inelastic neutron scattering spectra could be avoided for low $E_i - E_f$. The peak values in the neutron scattering spectra were fit with a Lorentzian peak profile function to determine the dispersion of spin waves in q. The parameters Δ and D were obtained by fitting the measured dispersion with Eq. (5). Accordingly, the energy gap at the ZC was found to be $\Delta = 214 \pm 80\,\mu$eV, and the slope of the dispersion $D = 242 \pm 11$ meV Å^2.

The MCA and the magnetic spin wave dispersion at low q were also evaluated using first-principles calculations for comparison with the inelastic neutron scattering measurements. We have used fully relativistic Korringa-Kohn-Rostoker [51] coherent-potential approximation (KKR-CPA) [52–54] method for electronic structure calculations for both ordered and disordered compounds, where for the later, the CPA is used to account for the effects of disorder on the electronic structure and energetics. The Ni-Mn-Ga system can be considered to have uniaxial magnetocrystalline anisotropy [25], which is calculated as the difference between the energies of the compound with the magnetic moment ordered either along the direction [010] or [101]. The MCA was calculated by both a direct difference between the energies of two magnetic moment orientations and using the magnetic torque approach [55], within the fully relativistic KKR [51] CPA [52–54] method, as implemented in SPRKKR code [56,57]. The calculations have been performed using the local spin density approximation (LDA) to density functional theory (DFT) and the Vosko-Wilk-Nusair parameterization of the exchange correlation function [58]. The energy integration was executed over 32 points in complex energies plane. In order to verify the convergence of the MCA, the Brillouin zone (BZ) summations over special k-points were carried up to $50 \times 50 \times 50$-k-points mesh. The MCA is changed by less than 3% with further increase in the number of k-points. The difference between MCA obtained by direct and magnetic torque methods is less than 1%.

The calculated MCA or Δ is accordingly found to be $\sim 80\,\mu$eV for stoichiometric Ni_2MnGa and $\sim 120\,\mu$eV for off-stoichiometric $Ni_2Mn_{1.14}Ga_{0.86}$. Our result is somewhat lower compared with the result of $\sim 180\,\mu$eV obtained by Enkovaara *et al.* for stoichiometric Ni_2MnGa [47]. Using the rigid band model to account for off-stoichiometry, they furthermore obtained an MCA of $\sim 60\,\mu$eV for $Ni_2Mn_{1.14}Ga_{0.86}$ [47]. In their study, Enkovaara *et al.* used a scalar relativistic approach to solve the Dirac equation and the spin-orbit coupling was treated within the second order variational method. In addition, the MCA was calculated within the frozen potential approximation. Both these approaches have limited validity. In off-stoichiometric $Ni_2Mn_{1.14}Ga_{0.86}$, the Ga and Mn atoms randomly occupy the Ga sublattice. Because the scattering properties of Ga and Mn atoms are significantly different, weak scattering approximations such as the rigid-band and virtual crystal approximations fail to describe the effects of disorder on the electronic structure, while these effects are properly accounted for within the CPA [53,54]. As a result, results from the rigid band approach [47] and CPA differ from each other both in magnitude and concentration dependence: in the rigid band approach the MCA is reduced from 180 to
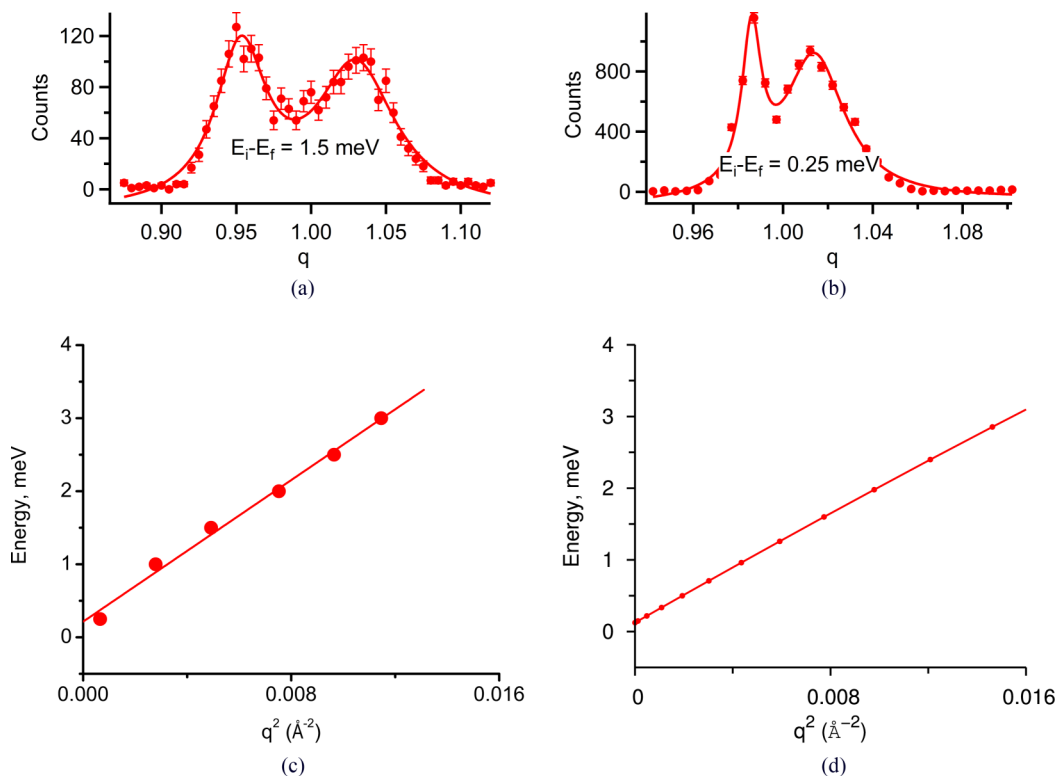
FIG. 6. (Color online) Representative scans for inelastic neutron scattering measurements at 250 K in the constant energy transfer mode showing peaks corresponding to the magnetic spin waves in the martensite phase, for (a) $E_i - E_f = 1.5$ meV and (b) $E_i - E_f = 0.25$ meV. Spin wave dispersion near the zone center (ZC) for the Ni-Mn-Ga alloy: (c) determined from neutron scattering measurements and (d) obtained from first-principles calculations.

60 μeV, while, in CPA the result for MCA is increased from 80 to 120 μeV. The value of MCA obtained from our calculations is closer to the range obtained from spin wave measurements, as described above.

Moreover, we used a combination of first-principles and model approaches to describe the spin wave dispersions. In this approach, the magnetic system is described by a Heisenberg Hamiltonian with exchange constants J_{ij} that describe the interaction of classical magnetic moments localized on sites i and j [59,60]. The J_{ij} were calculated using the expression obtained by employing the linear response technique in the framework of the multiple scattering formalism [61,62]. The J_{ij} describe magnetic excitations of the initially collinear magnetically ordered state. Previously, this approach was successfully applied to describe properties of magnetic excitations in Heusler alloys [63–66]. The CPA was employed to calculate the electronic structure and corresponding Green function of the off-stoichiometric Ni-Mn-Ga alloy. Furthermore, we used the first-principles-determined J_{ij}s to calculate the spin wave dispersions of a disordered Heisenberg binary system in the spirit of the approach proposed in Refs. [67,68] in the lowest approximation to the spin Green function, which in turn corresponds to the virtual crystal approximation (VCA) (for further details, please see Supplemental Material [39]; Refs. [69–75]). Since the Ni magnetic moments cannot be described as rigid and the Ni sublattice cannot support magnons [66], we only consider Mn–Mn interactions in the Heisenberg Hamiltonian. The calculated spin wave

dispersion curve is shown in Fig. 6(d). The value for D from first-principle calculations is $\sim$210 meV Å^2, which is also in fair agreement with the results from inelastic neutron scattering measurements.

Since the results from both the first-principle calculations and spin wave measurements are consistent with each other within the experimental error margins, we have used the K_u values obtained from them for further calculations of the free energy density.

C. Prediction of ϕ from phenomenological model

As explained in Sec. III.A., the angle of rotation of the magnetic moments ϕ within twin variant I, for an applied magnetic field of $\vec{H}$ and concurrent with a reoriented twin volume fraction of f, can be predicted from Eq. (4) by noting the point in the free energy surface where U is minimum or $\partial U / \partial \phi = 0$. For the purpose of predicting ϕ, we can exclude E_{int}, which is a constant.

The total free energy density (without E_{int}) as functions of f, ϕ, and H, is calculated from Eq. (4) by using the values of M_S and K_u that are described in the previous section. Furthermore, $f \sim 0.6$ is used, which is determined from *in situ* polarized neutron diffraction measurements at $H = 0.5$ T. The results are shown in Figs. 7(a)–7(c) for three different values of K_u: (a) $K_u = 120 \mu$eV, which corresponds to the value obtained from first-principle calculations; (b) $K_u = 135 \mu$eV, which is the lower limit of the value determined from neutron
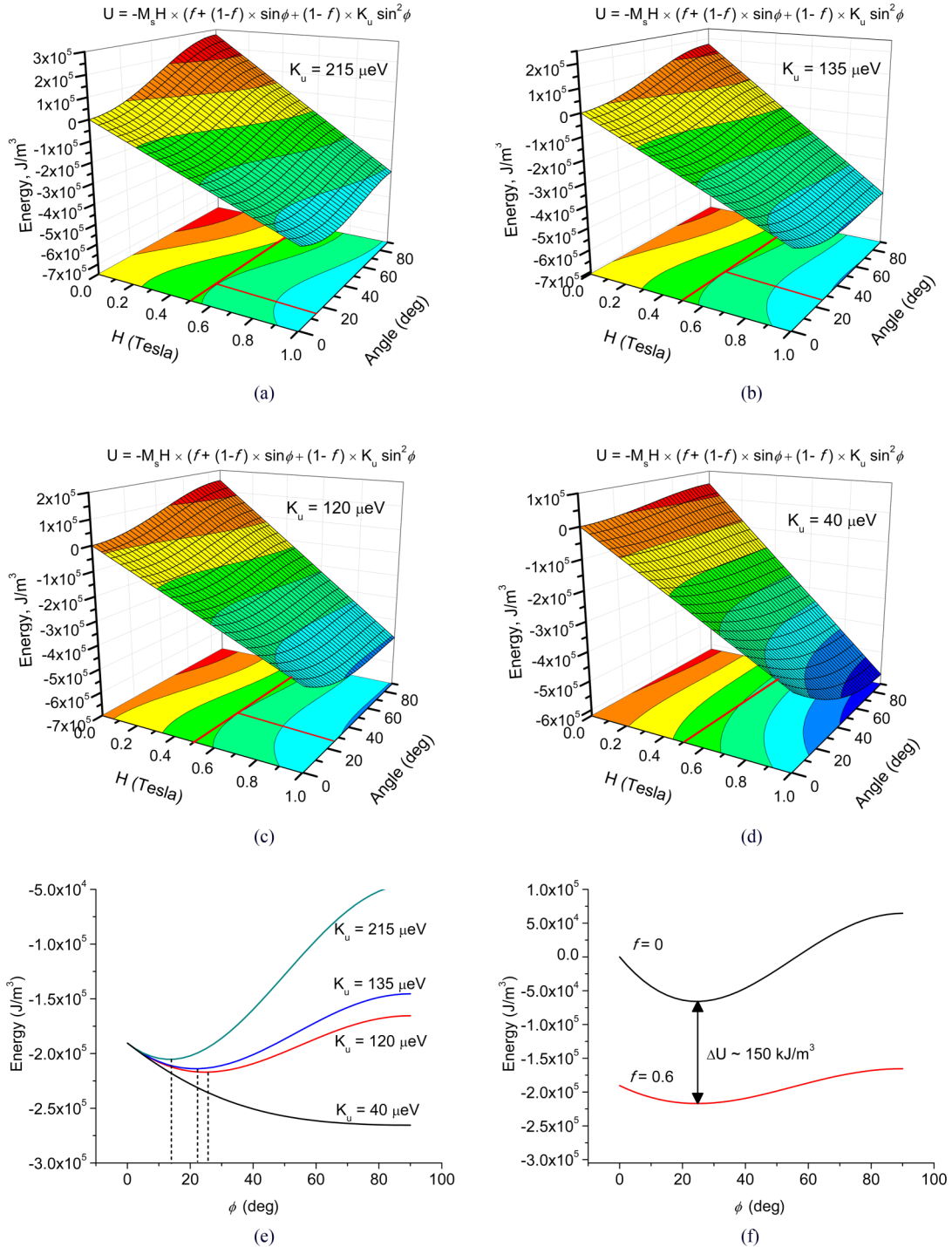
FIG. 7. (Color online) The free energy surfaces calculated from Eq. (4) for reoriented twin volume fractions of $f \sim 0.6$, using values of (a) $K_u = 215\,\mu$eV, (b) $K_u = 135\,\mu$eV, (c) $K_u = 120\,\mu$eV, and (d) $K_u = 40\,\mu$eV. (e) The constant H slices at $H = 0.5$ T calculated with different K_u values. (f) The constant H slices at $H = 0.5$ T calculated with $K_u = 120\,\mu$eV, for $f = 0$ and $f = 0.6$, shows that the energy difference between the two states is given by $\Delta U \sim 150\,$kJ/m^3.

scattering measurement of spin waves; and (c) $K_u = 215\,\mu$eV, which is the median value determined from neutron scattering measurement of spin waves.

We note that Figs. 7(a)–7(c) are qualitatively similar. The dotted lines on the bottom contours in these figures depict the loci for the minimum point in the free energy surface as functions of field strength H and the rotation angle of

the magnetic moments ϕ. Therefore, for a specific volume fraction of reoriented twins f, ϕ is expected to vary with magnetic field H following the locus of the minimum in the free energy surface. Accordingly, Figs. 7(a)–7(c) show that ϕ has a linear dependence on H at lower fields but eventually becomes nonlinear with increasing magnetic fields. For a magnetic field strength of $H = 0.5$ T, the minimum in the free

energy surface is at $\phi \sim 15°$ for $K_u = 215\,\mu$eV, $\phi \sim 22°$ for $K_u = 135\,G\,\mu$eV, and $\phi \sim 25°$ for $K_u = 120\,\mu$eV, as shown in Fig. 7(e), which are fairly close to each other, although ϕ predicted from $K_u = 215\,\mu$eV is slightly in the lower range. The predictions of $\phi \sim 22° - 25°$ are consistent with the value of $\phi \sim 35°$ determined from polarized neutron scattering experiments. Therefore, we find that the phenomenological expression for the free energy density as shown in Eq. (4), which although appears simple, can provide a useful and consistent definition for physical correlation between twin reorientation fractions and rotation angle of magnetic moments in an FSMA crystal under applied magnetic fields.

We however note that, if $K_u = 40\,\mu$eV is used (this value was obtained from magnetization curves measured for a bulk crystal), the free energy surface is qualitatively different, as shown in Fig. 7(d). For this later case, the free energy surface now shows no minimum in the free energy curve for $H = 0.5$ T, which would predict instability and a complete rotation of the magnetic moment to $\phi = 90°$, a scenario that is inconsistent with all experimental observations. This clearly demonstrates the significance of a correct determination of M_S and K_u towards predicting the transient magnetic and structural states at intermediate field strengths in FSMAs, which we achieved here using high-resolution neutron scattering measurements of spin waves and fully relativistic first-principles calculations.

D. Interfacial energy for twin boundary propagation

Finally, we turn our attention to the estimation of the interfacial energy E_{int} based on the difference in the free energy densities for $f = 0$ and $f = 0.6$, as explained in Sec. IV.A. Figure 7(f) shows the difference between the calculated free energy densities for $f = 0$ and $f = 0.6$ at their minima, which are obtained using $K_u = 120\,\mu$eV. The difference in the minima of the free energy curves, $\Delta U \sim 150\,$kJ/m^3, should be the interfacial energy E_{int} that is spent partly for nucleation of twin boundaries and partly for twin boundary motion.

Since we observed the initiation of twin reorientation at the threshold field of $H = 0.5$ T, it is clear that mostly motion of type I twin boundaries is activated at this field [42]. These types of twin boundaries have twinning planes of the $(1\bar{2}\bar{1})$ type (following the monoclinic notation used here) and a misorientation angle of $\sim 86°$ between the easy magnetization axes across the twin boundaries [76–78]. Based on quasi-static compression experiments on single-crystal Ni-Mn-Ga FSMA samples, the critical driving force required to initiate motion of type I twin boundaries was estimated earlier to be $\sim 50-75\,$kJ/m^3 at low travelling velocities [79]. The estimate of E_{int} is $\sim 150\,$kJ/m^3 for magnetoelastic twin boundary propagation in Ni-Mn-Ga FSMA, which we obtained here based on direct observations of microscopic magnetostructural changes, is therefore consistent with similar estimates obtained earlier through indirect means.

V. SUMMARY

In summary, we demonstrated the application of polarized neutron diffraction as a powerful *in situ* characterization tool for directly measuring the simultaneous rotation of magnetic moments and twin reorientation in a Ni-Mn-Ga FSMA. The technique in general should also have potential applications for characterizing similarly complex magnetostructural changes in other multiferroic materials. The experimentally observed correlation between twin reorientation fraction and the rotation angle of magnetic moments is also consistently modeled using a phenomenological expression for the total free energy density. However, such modeling critically depends on using the correct value for the fundamental magnetoelastic coupling constant of K_u, which we obtained here directly using both high-resolution inelastic neutron scattering measurements of spin waves and from fully relativistic first-principles calculations. Furthermore, by analyzing the directly measured magnetostructural changes, we could estimate that the interfacial energy for magnetic-field-induced twin boundary motion in this material is $\sim 150\,$kJ/m^3.

The future design of FSMAs as reliable material components in smart magnetic devices will depend on having an accurate knowledge of magnetic-field-induced microscopic magnetostructural changes, which in turn are decided by a delicate energy balance between K_u or MCA and the energy required for magnetoelastic twin boundary motion. The use of the state-of-the-art tools for *in situ* characterization and fully relativistic first-principles calculations, as presented here, will be indispensable for an accurate description of these variables.

[1] R. Kainuma, Y. Imani, W. Ito, Y. Sutou, H. Morito, S. Okamoto, O. Kitakami, K. Oikawa, A. Fujita, T. Kanomata, and K. Ishida, Nature **439**, 957 (2006).

[2] S. Geprägs, M. Opel, S. T. B. Goennenwein, and R. Gross, Philos. Mag. Lett. **87**, 141 (2007).

[3] S. H. Baek, H. W. Jang, C. M. Folkman, Y. L. Li, B. Winchester, J. X. Zhang, Q. He, Y. H. Chu, C. T. Nelson, M. S. Rzchowski, X. Q. Pan, R. Ramesh, L. Q. Chen, and C. B. Eom, Nat. Mater. **9**, 309 (2010).

[4] C. S. Watson, C. Hollar, K. Anderson, W. B. Knowlton, and P. Müllner, Adv. Funct. Mater. **23**, 3995 (2013).

[5] D. C. Dunand and P. Müllner, Adv. Mater. **23**, 216 (2011).

[6] A. N. Lavrov, S. Komiya, and Y. Ando, Nature **418**, 385 (2002).

[7] M. Chmielus, X. X. Zhang, C. Witherspoon, D. C. Dunand, and P. Müllner, Nat. Mater. **8**, 863 (2009).

[8] P. Müllner, V. A. Chernenko, and G. Kostorz, J. Appl. Phys. **95**, 1531 (2004).

[9] P. Müllner, V. A. Chernenko, M. Wollgarten, and G. Kostorz, J. Appl. Phys. **92**, 6708 (2002).

[10] A. Sozinov, Y. Ezer, G. Kimmel, P. Yakovenko, D. Giller, Y. Wolfus, Y. Yeshurun, K. Ulakko, and V. K. Lindroos, J. Phys. IV **11**, 311 (2001).

[11] A. Sozinov, A. A. Likhachev, N. Lanska, K. Ullakko, and V. K. Lindroos, J. Phys. IV **112**, 955 (2003).

[12] K. Ullakko, J. K. Huang, C. Kantner, R. C. O'Handley, and V. V. Kokorin, Appl. Phys. Lett. **69**, 1966 (1996).

[13] E. Faran and D. Shilo, J. Mech. Phys. Solids **59**, 975 (2011).

[14] A. Pramanick, X.-L. Wang, A. D. Stoica, C. Yu, Y. Ren, S. Tang, and Z. Gai, Phys. Rev. Lett. **112**, 217205 (2014).

[15] V. A. Chernenko, V. A. L'vov, P. Müllner, G. Kostorz, and T. Takagi, Phys. Rev. B **69**, 134410 (2004).

[16] R. C. O'Handley, J. Appl. Phys. **83**, 3263 (1998).

[17] O. Heczko, K. Jurek, and K. Ullakko, J. Magn. Magn. Mater. **226**, 996 (2001).

[18] I. Aaltio, O. Soderberg, Y. L. Ge, and S. P. Hannula, Scripta Mater. **62**, 9 (2010).

[19] C. M. Landis, J. Mech. Phys. Solids **56**, 3059 (2008).

[20] Y. W. Lai, R. Schafer, L. Schultz, and J. McCord, Acta Mater. **56**, 5130 (2008).

[21] A. Neudert, Y. W. Lai, R. Schäfer, M. Kustov, L. Schultz, and J. McCord, Adv. Eng. Mater. **14**, 601 (2012).

[22] A. Neudert, Y. W. Lai, R. Schäfer, and J. McCord, in *Proceedings of the International Conference and Exhibition on New Actuators and Drive Systems*, edited by H. Borgmann (WFB Wirtschaftsförderung Bremen GmbH, Bremen, 2010), p. 762.

[23] P. Müllner, V. A. Chernenko, and G. Kostorz, J. Magn. Magn. Mater. **267**, 325 (2003).

[24] H. D. Chopra, C. H. Ji, and V. V. Kokorin, Phys. Rev. B **61**, R14913 (2000).

[25] L. Straka and O. Heczko, J. Appl. Phys. **93**, 8636 (2003).

[26] O. Heczko, L. Straka, V. Novak, and S. Fähler, J. Appl. Phys. **107**, 09A914 (2010).

[27] R. Tickle and R. D. James, J. Magn. Magn. Mater. **195**, 627 (1999).

[28] V. A. Chernenko, S. P. Zagorodnyuk, V. A. L'vov, R. C. O'Handley, and Y. Kono, J. Appl. Phys. **99**, 103906 (2006); C. P. Sasso, V. A. L'vov, V. A. Chernenko, J. M. Barandiaran, M. Pasquale, and Y. Kono, Phys. Rev. B **81**, 224428 (2010).

[29] A. Budruk, C. Phatak, A. K. Petford-Long, and M. De Graef, Acta Mater. **59**, 4895 (2011).

[30] N. I. Glavatska, A. A. Rudenko, N. Glavatskiy, and V. A. L'vov, J. Magn. Magn. Mater. **265**, 142 (2003).

[31] A. A. Likhachev, A. Sozinov, and K. Ullakko, Mater. Sci. Engg. A: Struct. **378**, 513 (2004).

[32] J. Y. Li and Y. F. Ma, Mech. Mater. **40**, 1022 (2008).

[33] Y. F. Ma and J. Y. Li, Acta Mater. **55**, 3261 (2007).

[34] Y. F. Ma and J. Y. Li, Appl. Phys. Lett. **90**, 172504 (2007).

[35] A. Pramanick, X. P. Wang, K. An, A. D. Stoica, J. Yi, Z. Gai, C. Hoffmann, and X.-L. Wang, Phys. Rev. B **85**, 144412 (2012).

[36] A. Pramanick, K. An, A. D. Stoica, and X.-L. Wang, Scripta Mater. **65**, 540 (2011).

[37] A. Pramanick, V. Lauter, X.-L. Wang, K. An, H. Ambaye, R. J. Goyette Jr, J. Yi, Z. Gai, and A. D. Stoica, J. Appl. Crystallogr. **45**, 1024 (2012).

[38] G. L. Squires, *Introduction to the Theory of Thermal Neutron Scattering* (Dover Publications Inc., Mineola, New York, 1996).

[39] See Supplemental Material at http://link.aps.org/supplemental/10.1103/PhysRevB.92.134109 for method to correct for neutron beam depolarization and additional details on first-principles calculations.

[40] A. R. Wildes, Rev. Sci. Instrum. **70**, 4241 (1999).

[41] O. Heczko, J. Magn. Magn. Mater. **290**, 787 (2005); L. Straka and O. Heczko, *ibid.* **290**, 829 (2005).

[42] O. Heczko, L. Straka, I. Aaltio, and S. P. Hannula, Mater. Sci. Engg. A: Struct. **481**, 283 (2008).

[43] O. Heczko, V. Kopecky, A. Sozinov, and L. Straka, Appl. Phys. Lett. **103**, 072405 (2013).

[44] L. Straka, O. Heczko, and H. Hanninen, Acta Mater. **56**, 5492 (2008).

[45] R. C. O'Handley, S. J. Murray, M. Marioni, H. Nembach, and S. M. Allen, J. Appl. Phys. **87**, 4712 (2000).

[46] R. C. O'Handley, *Modern Magnetic Materials* (John Wiley & Sons, New York, NY, 2000).

[47] J. Enkovaara, A. Ayuela, L. Nordstrom, and R. M. Nieminen, Phys. Rev. B **65**, 134422 (2002).

[48] V. Runov and U. Stuhr, J. Magn. Magn. Mater. **323**, 244 (2011).

[49] C. Kittel, *Introduction to Solid State Physics*, 8th ed. (John Wiley & Sons, Hoboken, NJ, 2005).

[50] U. Stuhr, P. Vorderwisch, and V. V. Kokorin, Physica B **234**, 135 (1997).

[51] J. Korringa, Physica **13**, 392 (1947); W. Kohn and N. Rostoker. Phys. Rev. **94**, 1111 (1954).

[52] B. Velický, S. Kirkpatrick, and H. Ehrenreich, Phys. Rev. **175**, 747 (1968).

[53] G. M. Stocks, W. M. Temmerman, and B. L. Gyorffy, Phys. Rev. Lett. **41**, 339 (1978).

[54] S. V. Beiden, N. E. Zein, and G. D. Samolyuk, J. Phys.: Condens. Matter **3**, 9651 (1991).

[55] J. B. Staunton, L. Szunyogh, A. Buruzs, B. L. Gyorffy, S. Ostanin, and L. Udvardi, Phys. Rev. B **74**, 144411 (2006).

[56] The Munich SPR-KKR package, version 6.3, H. Ebert *et al.* http://ebert.cup.uni-muenchen.de/SPRKKR.

[57] H. Ebert and D. Ködderitzsch, J. Minár: Rep. Prog. Phys. **74**, 96501 (2011).

[58] S. H. Vosko, L. Wilk, and M. Nusair, Can. J. Phys. **58**, 1200 (1980).

[59] V. G. Vaks and N. E. Zein, Sov. Phys. JETP **40**, 537 (1975).

[60] V. G. Vaks and G. D. Samolyuk, Phys. JETP **88**, 89 (1999).

[61] A. I. Liechtenstein, M. I. Katsnelson, V. P. Antropov, and V. A. Gubanov, J. Magn. Magn. Mater. **67**, 65 (1987).

[62] M. van Schilfgaarde and V. P. Antropov, J. Appl. Phys. **85**, 4827 (1999).

[63] V. D. Buchelnikov, V. V. Sokolovskiy, H. C. Herper, H. Ebert, M. E. Gruner, S. V. Taskaev, V. V. Khovaylo, A. Hucht, A. Dannenberg, M. Ogura, H. Akai, M. Acet, and P. Entel, Phys. Rev. B **81**, 094411 (2010).

[64] I. Galanakis and E. Sasioglu, J. Phys. D: Appl. Phys. **44**, 235001 (2011).

[65] I. Galanakis and E. Sasioglu, J Mater. Sci. **47**, 7678 (2012).

[66] Y. Kurtulus, R. Dronskowski, G. D. Samolyuk, and V. P. Antropov, Phys. Rev. B **71**, 014425 (2005).

[67] G. X. Tang and W. Nolting, Phys. Rev. B **73**, 024415 (2006).

[68] A. Theumann, J. Phys. C: Solid State **7**, 2328 (1974).

[69] A. Theumann and R. A. Tahir-Kheli, Phys. Rev. B **12**, 1796 (1975).

[70] G. Bouzerar and P. Bruno, Phys. Rev. B **66**, 014410 (2002).

[71] G. X. Tang and W. Nolting, Phys. stat. sol. (b) **244**, 735 (2007).

[72] G. D. Samolyuk, B. P. T. Fokwa, R. Dronskowski, and G. J. Miller, Phys. Rev. B **76**, 094404 (2007).

[73] O. K. Andersen and O. Jepsen, Phys. Rev. Lett. **53**, 2571 (1984).

[74] N. J. Ramer and A. M. Rappe, Phys. Rev. B **62**, R743(R) (2000).

[75] P. Buczek, A. Ernst, P. Bruno, and L. M. Sandratskii, Phys. Rev. Lett. **102**, 247206 (2009).

[76] D. Y. Cong, Y. D. Zhang, Y. D. Wang, C. Esling, X. Zhao, and L. Zuo, J. Appl. Cryst. **39**, 723 (2006).

[77] Z. Li, Y. Zhang, C. Esling, X. Zhao, Y. Wang, and L. Zuo, J. Appl. Cryst. **43**, 617 (2010).

[78] Z. Li, Y. Zhang, C. Esling, X. Zhao, and L. Zuo, Acta Mater. **59**, 3390 (2011).

[79] E. Faran and D. Shilo, Appl. Phys. Lett. **100**, 151901 (2012).